

Anisotropic superconducting gaps in YNi₂B₂C: A first-principles investigationMitsuaki Kawamura,^{1,*} Ryosuke Akashi,² and Shinji Tsuneyuki^{1,2}¹*Institute for Solid State Physics, The University of Tokyo, Kashiwa 277-8581, Japan*²*Department of Physics, The University of Tokyo, Tokyo 113-0033, Japan*

(Received 29 September 2016; revised manuscript received 6 January 2017; published 14 February 2017)

We calculate superconducting gaps and quasiparticle density of states of YNi₂B₂C in the framework of the density functional theory for superconductors to investigate the origin of highly anisotropic superconducting gaps in this material. Calculated phonon frequencies, the quasiparticle density of states, and the transition temperature show good agreement with experimental results. From our calculation of superconducting gaps and orbital character analysis, we establish that the orbital character variation of the Fermi surface is the key factor of the anisotropic gap. Since the electronic states that consist of mainly Ni 3*d* orbitals couple weakly with phonons, the superconducting gap function is suppressed for the corresponding states, which results in the anisotropy observed in the experiments. These results are hints to increase the transition temperature of materials in the borocarbide family.

DOI: [10.1103/PhysRevB.95.054506](https://doi.org/10.1103/PhysRevB.95.054506)**I. INTRODUCTION**

Superconductors exhibiting an anisotropic gap have attracted continuous attention for their possible exotic superconducting mechanisms. Unconventional mechanisms, which are completely different from the phonon mechanism established by the Bardeen-Cooper-Schrieffer (BCS) [1] and Eliashberg [2] theories, have been extensively discussed for the nodal *d*- and *p*-wave gaps in cuprate, iron-based, and heavy-fermion superconductors [3–5], etc. In view of this history, YNi₂B₂C [6,7] is recently getting a surge of interest since its superconducting gap is significantly anisotropic. Polynomial temperature dependence of its specific-heat coefficient has been observed ($C_p \propto T^3$), suggesting nodal structure of the gap. The strong anisotropy of the gap has also been indicated in the magnetic-field dependence of C_p [8–10], broad peak in the tunneling conductance spectrum [11], in-plane anisotropy in the ultrasonic attenuation [12] and Doppler shift measurements [13], and large anisotropic gap ratio ($\Delta_{\max}/\Delta_{\min} = 2.1$), namely, the ratio of the maximum to the minimum of the gap in the reciprocal space, observed with angle-resolved photoemission spectroscopy measurement [14]. Strong anti-ferromagnetic spin fluctuation has been revealed from pulsed NMR studies [15], which suggests that electronic correlation has a role.

Although significant magnetic characteristics are generally observed in the rare-earth nickel borocarbide family, the yttrium systems seems exceptional. Among $LnNi_2B_2C$ ($Ln =$ lanthanide), the Pr [16], Nd [17], Sm [18], Gd [19], and Tb [20] systems exhibit magnetic order, whereas in the Dy [21], Ho [22], Er [23], and Tm [24] systems both magnetic orders and superconducting transition have been observed. Previous first-principles investigations [25,26] revealed that the magnetic orders in those materials are caused by the Ruderman-Kittel-Kasuya-Yosida interaction [27–29] between localized spin from 4*f* electrons. In the Y system, on the other hand, the yttrium sites, whose valence states are less localized 4*d* and 5*s* orbitals, do not show magnetic order. This

implies that the effective description of electronic states in the Y systems should be different from the other rare-earth systems.

As a matter of fact, a relevance of the conventional phonon-mediated superconducting mechanism has also been experimentally indicated. First, the isotope effect of boron atom has been observed [30,31] in this material. Moreover, softening of the transverse acoustic (TA) phonon mode occurs, which is likely due to strong electron-phonon coupling [32]. The apparent coexistence of the strong electron-phonon coupling and the gap anisotropy invites us to a fundamental question: Can the conventional superconducting mechanism realize such an anisotropic gap? Although the conventional mechanism is generally regarded to induce an almost isotropic gap [33], there is no theory to prohibit the opposite. In a few multiband systems such as MgB₂ [34,35], the gap has different values for different bands, which can be explained with orbital dependence of the electron-phonon coupling. Even the nodal gap can theoretically emerge if we assume extreme *k*-point dependence of the electron-phonon coupling [36].

In this study, we investigate the possibility of the anisotropic superconductivity due to the conventional phonon mechanism in YNi₂B₂C in a fully *ab initio* manner. Recent progress in *ab initio* theories for superconductors, such as density functional theory for superconductors (SCDFT) [37,38] and anisotropic Migdal-Eliashberg theory [39], has enabled us to work on this issue. The standard method to calculate gaps of the superconducting phase induced by the phonon-mediated mechanism is to solve the Eliashberg equation. However, it is difficult to solve it in a fully nonempirical manner; because the interaction and the gap function depend both on the Kohn-Sham state and the frequency, formidable computational cost is required for solving this equation. On the other hand, in the density functional theory for superconductors, static anomalous density serves as a fundamental quantity, with which efficient numerical schemes can be implemented with reduced computational cost. In the recent SCDFT study, T_c as well as the tunneling gap have been reproduced from first principles [40]. We apply this method to the YNi₂B₂C system.

In Sec. II, we introduce the density functional theory for superconductors, which bases our first-principles calculations

*mkawamura@issp.u-tokyo.ac.jp

in this study. In Sec. III, we present the numerical method to calculate superconducting properties such as the superconducting gap. We here append a specific scheme to treat the k -dependent anisotropy precisely. In Sec. IV, we show the resulting electronic and phononic structure of $\text{YNi}_2\text{B}_2\text{C}$: the band structure, Fermi surfaces, superconducting gap function, phonon dispersion, superconducting transition temperature, and the quasiparticle density of states. We compare them with the corresponding experimental results. In Sec. V, we discuss the possible origin of the anisotropic superconducting gaps in $\text{YNi}_2\text{B}_2\text{C}$ within the conventional phonon-mechanism scenario. The summary and future prospects are given in Sec. VI.

II. THEORY

In this section, we present the formalism of density functional theory for superconductors (SCDFT) [37]; we can calculate superconducting properties such as the transition

temperature from first principles by using this method. In the current formalism of SCDFT with the decoupling approximation [38,41], we obtain the superconducting singlet order parameter as follows:

$$\chi(r, r') = \frac{1}{2} \frac{\Delta_{nk}}{\varepsilon_{nk}} \tanh\left(\frac{\beta \varepsilon_{nk}}{2}\right) \sum_{nk} \varphi_{nk}(r) \varphi_{nk}^*(r'), \quad (1)$$

where $\varepsilon_{nk} = \sqrt{\xi_{nk}^2 + \Delta_{nk}^2}$, $\varphi_{nk}(r)$ is the normal-state Kohn-Sham orbital having (nk) as the band index and the wave number, ξ_{nk} is the normal-state Kohn-Sham eigenenergy, and β is the inversed temperature. This order parameter is determined after we compute the electronic and lattice-dynamical properties by using the density functional calculations in the normal state. The Kohn-Sham gap function Δ_{nk} is calculated from the following gap equation:

$$\Delta_{nk} = -\frac{1}{2} \sum_{n'k'} K[V_{n'k'nk}]({g_{n'k'nk}}, \{\omega_{k'-k}\}, \xi_{nk}, \xi_{n'k'}) \tanh\left(\frac{\beta \varepsilon_{n'k'}}{2}\right) \frac{\Delta_{n'k'}}{\varepsilon_{n'k'}}, \quad (2)$$

$$K[V_{n'k'nk}]({g_{n'k'nk}}, \{\omega_{k'-k}\}, \xi_{nk}, \xi_{n'k'}) \equiv \frac{K^{\text{ep}}({g_{n'k'nk}}, \{\omega_{k'-k}\}, \xi_{nk}, \xi_{n'k'}) + K^{\text{ee}}[V_{n'k'nk}]({\xi_{nk}, \xi_{n'k'}})}{1 + Z({g_{n'k'nk}}, \{\omega_{k'-k}\}, \xi_{nk})}, \quad (3)$$

where $\{\omega_q\} \equiv \omega_{q1}, \dots, \omega_{qN_{\text{branch}}}$ are frequencies of phonons having q as the wave number, $\{g_{n'k'nk}\} \equiv g_{n'k'nk}^1, \dots, g_{n'k'nk}^{N_{\text{branch}}}$ are the vertices between a phonon and Kohn-Sham orbitals ($\varphi_{n'k'}, \varphi_{nk}$), and N_{branch} is the number of branches of phonons. Forms of the electron-phonon kernel K^{ep} and the renormalization Z are identical to that of previous studies [40,42,43]. K^{ee} is the electron-electron kernel as follows:

$$K^{\text{ee}}[V_{n'k'nk}]({\xi_{nk}, \xi_{n'k'}}) = \frac{2}{\pi} \int_0^\infty d\omega \frac{|\xi_{nk}| + |\xi_{n'k'}|}{(|\xi_{nk}| + |\xi_{n'k'}|)^2 + \omega^2} V_{n'k'nk}(\omega), \quad (4)$$

$$V_{n'k'nk}(\omega) \equiv \iint d^3r d^3r' \varphi_{nk}^*(r) \varphi_{n'k'}^*(r') V_{\text{scr}}(r, r', \omega) \varphi_{nk}(r') \varphi_{n'k'}(r), \quad (5)$$

where $V_{\text{scr}}(r, r', \omega)$ is the screened Coulomb interaction; we calculate it including the dynamical screening effect [43]. Neglecting the temperature dependence of K^{ee} considered in the previous study (Eq. (2) in Ref. [43]), we obtain Eq. (4). The numerical treatment of the integration in Eq. (4) is appended in Appendix A.

While $V_{\text{scr}}(r, r', \omega)$ is calculated by using the random phase approximation (RPA) in the previous study [43], we calculate it by using the adiabatic local density approximation [44] (ALDA) in this work as follows:

$$V_{\text{scr}}(r, r', \omega) = \frac{1}{|r - r'|} + \iint d^3r_1 d^3r_2 \left(\frac{1}{|r - r_1|} + \frac{\delta^2 E_{\text{XC}}}{\delta \rho(r) \delta \rho(r_1)} \right) \Pi(r_1, r_2, \omega) \frac{1}{|r_2 - r'|}, \quad (6)$$

where $\rho(r)$ is the charge density, E_{XC} is the exchange-correlation energy, $\Pi(r, r', \omega)$ is the polarization function given by the solution of the following equation

$$\Pi(r, r', \omega) = \Pi_0(r, r', \omega) + \iint d^3r_1 d^3r_2 \Pi_0(r, r_1, \omega) \left(\frac{1}{|r_1 - r_2|} + \frac{\delta^2 E_{\text{XC}}}{\delta \rho(r_1) \delta \rho(r_2)} \right) \Pi(r_2, r', \omega), \quad (7)$$

and $\Pi_0(r, r', i\omega)$ is the independent particle polarizability

$$\begin{aligned} & \Pi_0(r, r', \omega) \\ &= \sum_{nkn'k'} \frac{\theta(-\xi_{nk}) - \theta(\xi_{n'k'})}{\xi_{n'k'} - \xi_{nk} + i\omega} \varphi_{nk}^*(r) \varphi_{n'k'}^*(r') \varphi_{nk}(r') \varphi_{n'k'}(r), \end{aligned} \quad (8)$$

where $\theta(\xi)$ is the step function.

When we compare the calculated Δ_{nk} with the experiments, it must be noticed that Δ_{nk} is not theoretically guaranteed

to correspond to the experimental gap; while the former gives the gap in the Kohn-Sham Bogoliubov-de Gennes energy dispersion, the latter is defined with the poles of the electronic Green's function. Nevertheless, we discuss the gap anisotropy with the calculated Δ_{nk} on the basis of an assumption that it describes the experimental gap on the semiquantitative level. This is justified for the following reasons: (i) There is a suggestive relation between the SCDFT gap and those from the many body perturbation theory [45,46]. From dressed anomalous Green's function $F_{nk}^R(\omega)$ in the Nambu-Gor'kov formalism [47,48], let us redefine Δ_{nk} as

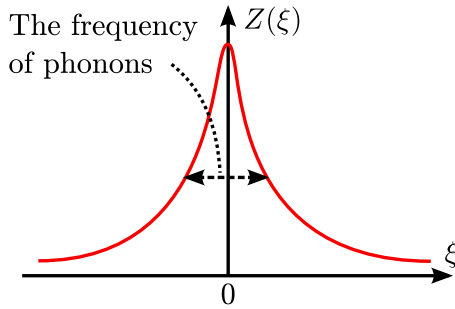


FIG. 1. Schematic illustration of the energy dependence of Z . This function has a strong energy dependence when $|\xi_{nk}|$ are equal to or lower than the phonon frequency.

follows:

$$\Delta_{nk} \equiv 2|\xi_{nk}| \int_0^{\infty} \frac{d\omega}{2\pi} \text{Im} F_{nk}^R(\omega). \quad (9)$$

Here, ξ_{nk} is the Kohn-Sham energy of the normal state. Remarkably, this redefined Δ_{nk} gap satisfies the equation similar to the SCDFD gap equation [46]. (ii) The “gap” $2\Delta_{nk}$ indeed agrees with the gap derived from the tunnel conductance for some materials [40,49]. If one wants to improve the precision of the analysis, dressed anomalous Green’s functions must be calculated from first principles based on the Eliashberg theory [2,50] or the G_0W_0 theory for superconductors [46,51], but it requires us to treat all the variables (k points, band indices, and Matsubara frequencies) explicitly. Since the numerical cost for such a calculation is unrealistically large, we do not address this improvement in this study.

III. NUMERICAL METHOD FOR THE GAP EQUATION

In this section, we explain the numerical method to compute the gap function [Eq. (2)], the independent particle polarizability [Eq. (8)], and the quasiparticle density of states

in a superconducting state. All these calculations concern the k -point integrations where the integrands have large values only in the vicinity of the Fermi level. We developed a method based on the tetrahedron interpolation for this difficulty.

A. Difficulty in the calculation of the gap equation

The renormalization factor Z and the electron-phonon XC kernel K^{ep} vary rapidly in the vicinity of Fermi surfaces. The origin of this rapid variation is strong energy ($\xi_{nk}, \xi_{n'k'}$) dependence of Z and K^{ep} in the vicinity of Fermi surfaces ($|\xi_{nk}|$ and $|\xi_{n'k'}|$ are equal to or lower than the phonon frequency; see Fig. 1). In order to treat this sensitive energy dependence precisely, we need an unrealistically large number of k points for solving the Kohn-Sham gap equation if we use the uniform grid.

In the previous works [41], randomly sampled k points have been used to perform the k integration in the gap equation; a large number of k points is adopted in the vicinity of Fermi surfaces. However, this method has two drawbacks. In the first place, it obviously yields a numerical error because of the random sampling. In the second place, it has a difficulty in the calculation of the density of states because we can not obtain exact weights of an integration including the delta function; for calculating such weights, we have to use the tetrahedron method [52] on sufficiently dense regular k grids (not on randomly sampled k points).

B. Deterministic solving via auxiliary gap function

To avoid this difficulty, we develop an alternative *deterministic* method that is free from the randomness and compatible with the tetrahedron method. We decouple the k dependence and energy dependence with a help of the auxiliary energy grid. Specifically, we define explicitly energy dependent auxiliary gap functions

$$\Delta_{nk}(\xi) \equiv -\frac{1}{2} \sum_{n'k'} K[V_{n'k'nk}]({g_{n'k'nk}}, \{\omega_{k'-k}\}, \xi, \xi_{n'k'}) \tanh\left(\frac{\beta \varepsilon_{n'k'}}{2}\right) \frac{\Delta_{n'k'}}{\varepsilon_{n'k'}}. \quad (10)$$

This auxiliary gap function satisfies $\Delta_{nk}(\xi_{nk}) = \Delta_{nk}$. Inserting $1 = \int d\xi' \delta(\xi' - \xi_{n'k'})$ into Eq. (10), we obtain simultaneous equations for the auxiliary gap function as follows:

$$\Delta_{nk}(\xi) = -\frac{1}{2} \int d\xi' \sum_{n'k'} \delta(\xi' - \xi_{n'k'}) K[V_{n'k'nk}]({g_{n'k'nk}}, \{\omega_{k'-k}\}, \xi, \xi') \tanh\left(\frac{\beta \varepsilon_{n'k'}(\xi')}{2}\right) \frac{\Delta_{n'k'}(\xi')}{\varepsilon_{n'k'}(\xi')}, \quad (11)$$

where $\varepsilon_{nk}(\xi) \equiv \sqrt{|\Delta_{nk}(\xi)|^2 + \xi^2}$. We use a sparse uniform k grid and nonuniform energy grid to solve this gap equation; the latter has much more points in the vicinity of $\xi = 0$ (Fig. 2).

Practically, the energy dependence of Z and K^{ep} becomes moderate when $\xi_{n'k'}$ is far from the Fermi level; we therefore introduce the integration with respect to $\xi_{n'k'}$ only for bands crossing the Fermi level as follows:

$$\begin{aligned} \Delta_{nk}(\xi) = & -\frac{1}{2} \int_{\xi_{\min}}^{\xi_{\max}} d\xi' \sum_{n'} \sum_{k'} \delta(\xi' - \xi_{n'k'}) K[V_{n'k'nk}]({g_{n'k'nk}}, \{\omega_{k'-k}\}, \xi, \xi') \tanh\left(\frac{\beta \varepsilon_{n'k'}(\xi')}{2}\right) \frac{\Delta_{n'k'}(\xi')}{\varepsilon_{n'k'}(\xi')} \\ & - \frac{1}{2} \sum_{n'} \sum_{k'}^{\text{Other}} K[V_{n'k'nk}]({g_{n'k'nk}}, \{\omega_{k'-k}\}, \xi, \xi_{n'k'}) \tanh\left(\frac{\beta \varepsilon_{n'k'}(\xi_{n'k'})}{2}\right) \frac{\Delta_{n'k'}(\xi_{n'k'})}{\varepsilon_{n'k'}(\xi_{n'k'})}, \end{aligned} \quad (12)$$

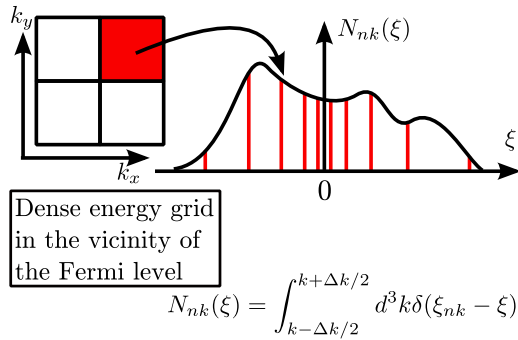


FIG. 2. Schematic illustration of the auxiliary energy grid. We use a smooth uniform k grid and dense nonuniform energy grid to solve this gap equation; the latter has much more points in the vicinity of $\xi = 0$.

where ξ_{\max} and ξ_{\min} are the maximum of the normal-state Kohn-Sham energy of bands crossing the Fermi level and minimum of that.

For evaluating the ξ integration in Eq. (12), we replace it with a discrete summation as $\int_{\xi_{\min}}^{\xi_{\max}} d\xi' \delta(\xi' - \xi_{n'k'}) \dots \approx \sum_i (d\xi)_i N_{n'k'}(\xi_i) \dots$. The energy grid $\{x_i\}$ is taken to be nonuniform as elaborated below. $N_{nk}(\xi_i)$ is the integration weight for each point (nki), which is calculated with the following procedure before solving the gap equation: (1) Calculate the Kohn-Sham energy eigenvalues on a k -point mesh denser than that used for the gap equation, (2) apply a tetrahedron-interpolation method to the k -point mesh and evaluate $N_{nk}(\xi_i)$, and (3) calculate optimum $N_{nk}(\xi_i)$ for the sparse k -point grid for the gap equation using a reverse interpolation method (Sec. III C 1).

We use the following energy grid and the weight of each point;

$$\xi_i = (x_i - x_{i_0}) \varepsilon_{\min} \frac{n_\xi}{2} \exp \left[a \left(|x_i - x_{i_0}| - \frac{2}{n_\xi} \right) \right], \quad (13)$$

$$(d\xi)_i = (dx)_i \left(1 + a |x_i - x_{i_0}| \right) \varepsilon_{\min} \frac{n_\xi}{2} \times \exp \left[a \left(|x_i - x_{i_0}| - \frac{2}{n_\xi} \right) \right], \quad (14)$$

where n_ξ is the number of energy grid ($i = 1, 2, 3, \dots, n_\xi$), and x_i and $(dx)_i$ are the representative point and the weight in the Gauss-Legendre quadrature ($-1 < x_i < 1$). We choose i_0 from $i = 1, 2, \dots, n_\xi$, so that the following factor is minimized:

$$\left| \xi_{\max} - (1 - x_{i_0}) \varepsilon_{\min} \frac{n_\xi}{2} \exp \left[a \left(1 - x_{i_0} - \frac{2}{n_\xi} \right) \right] \right| + \left| \xi_{\min} - (-1 - x_{i_0}) \varepsilon_{\min} \frac{n_\xi}{2} \exp \left[a \left(1 + x_{i_0} - \frac{2}{n_\xi} \right) \right] \right|, \quad (15)$$

where

$$a = \max \left[\frac{1}{1 - x_{i_0} - 2/n_\xi} \ln \left(\frac{\xi_{\max}}{(1 - x_{i_0}) \varepsilon_{\min} n_\xi / 2} \right), \frac{1}{1 + x_{i_0} - 2/n_\xi} \ln \left(\frac{-\xi_{\min}}{(1 + x_{i_0}) \varepsilon_{\min} n_\xi / 2} \right) \right]. \quad (16)$$

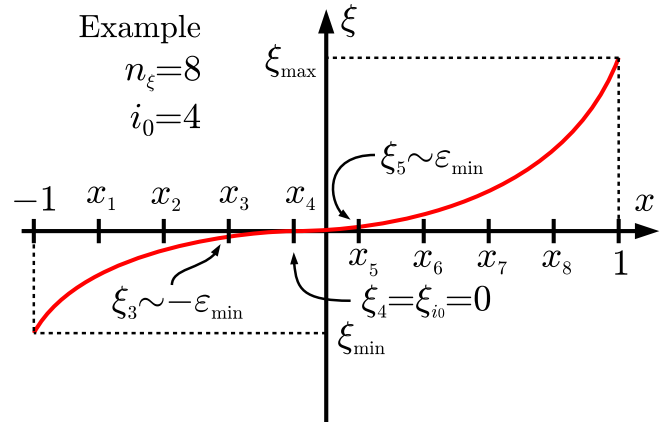


FIG. 3. A schematic illustration of the energy grid. It is represented in Eqs. (13) and (14); we can easily control the accuracy by tuning parameters in those equations.

This energy grid has the following properties (see Fig. 3):

- (1) It ranges between ξ_{\min} and ξ_{\max} .
- (2) The minimum energy scale is ε_{\min} .

Then, we can easily control the accuracy by tuning n_ξ and ε_{\min} .

By using the auxiliary energy grid, we can calculate the quasiparticle density of states (QPDOS) in a superconducting state as follows:

$$N_S(\varepsilon) = \sum_{nk} \delta(\varepsilon - \varepsilon_{nk}) = \sum_{nk} \int d\xi \delta(\xi - \xi_{nk}) \delta(\varepsilon - \varepsilon_{nk}(\xi)) \approx \sum_{nki} (d\xi)_i N_{nk}(\xi_i) \delta(\varepsilon - \varepsilon_{nk}(\xi_i)). \quad (17)$$

The four-dimensional (\mathbf{k} and i) integration in Eq. (17) is performed by using the pentachoron scheme (see Sec. III C 2).

C. Details of k integrations

1. Reverse interpolation of weight

We consider the k integration as follows:

$$\langle X \rangle = \sum_k X_k w(\varepsilon_k). \quad (18)$$

If this integration has the following conditions, it is efficient to interpolate X_k into a denser k grid and evaluate that integration in a dense k grid.

- (1) $w(\varepsilon_k)$ is sensitive to ε_k (e.g., the step function, the delta function, etc.) and requires ε_k on a dense k grid.
- (2) The numerical cost to obtain X_k is much larger than that to obtain ε_k (e.g., the polarization function).

This method is performed as follows:

- (1) We calculate ε_k on a dense k grid.
- (2) We calculate X_k on a coarse k grid and obtain that on a dense k grid by using the linear interpolation, the polynomial interpolation, the spline interpolation, etc.

$$X_k^{\text{dense}} = \sum_{k'}^{\text{coarse}} F_{kk'} X_{k'}^{\text{coarse}} \quad (19)$$

(3) We evaluate that integration in the dense k grid.

$$\langle X \rangle = \sum_k^{\text{dense}} X_k^{\text{dense}} w_k^{\text{dense}} \quad (20)$$

When X_k is a multicomponent array, e.g., $X_k = \varphi_k^*(r)\varphi_{k+q}^*(r')\varphi_k(r')\varphi_{k+q}(r)$ for Eq. (8), the computational cost for evaluating Eq. (19) and the memory size for X_k^{dense} become very large. To avoid this difficulty, we developed a method to obtain the result identical to the above result without interpolating X_k into a dense k grid. Namely, we calculate the integration weight on a coarse k grid from that on a dense k grid; we call it reverse interpolation. Therefore, if we require

$$\sum_k^{\text{dense}} X_k^{\text{dense}} w_k^{\text{dense}} = \sum_k^{\text{coarse}} X_k^{\text{coarse}} w_k^{\text{coarse}}, \quad (21)$$

we obtain

$$w_k^{\text{coarse}} = \sum_k^{\text{dense}} F_{k'k} w_{k'}^{\text{dense}}. \quad (22)$$

The numerical procedure for this method is as follows:

(1) We calculate the integration weight on a dense k grid w_k^{dense} from ε_k on that grid.

(2) We obtain the integration weight on a coarse k grid (w_k^{coarse}) by using the reverse interpolation method.

(3) We evaluate that integration in a coarse k grid where X_k was calculated.

This reverse interpolation method is employed in evaluating Eqs. (8), (12), and (17).

2. Four-dimensional numerical integration scheme for DOS

For evaluating accurately the four-dimensional integration in Eq. (17), we construct a method by extending the tetrahedron method to the four-dimensional case. We consider the following integration:

$$\langle X \rangle = \int_{\text{BZ}} d^3k \int d\xi X_k(\xi) \delta(\varepsilon - \varepsilon_k(\xi)), \quad (23)$$

where $X_k(\xi)$ and $\varepsilon_k(\xi)$ are smooth functions of k and ξ ; in the calculation of the QPDOS, $X_k(\xi) = N_{nk}(\xi)$ and $\varepsilon_k(\xi) = \sqrt{\Delta_{nk}^2(\xi) + \xi^2}$.

We divide four-dimensional (k, ξ) space into $24 \times N_k \times (N_\xi - 1)$ pentachora. If we assume $X_k(\xi)$ and $\varepsilon_k(\xi)$ as linear functions of k and ξ in each pentachoron, we can obtain the following result of Eq. (23) in a pentachoron.

$$\langle X \rangle_P \approx \frac{S_{\varepsilon_k(\xi)=\varepsilon}}{|\nabla_{k,\xi} \varepsilon_k(\xi)|} \langle X_k(\xi) \rangle_{\varepsilon_k(\xi)=\varepsilon} \equiv \sum_{i=1}^5 w_i X_i, \quad (24)$$

where $S_{\varepsilon_k(\xi)=\varepsilon}$ is the volume of the region in which $\varepsilon_k(\xi)$ becomes ε , $\langle X_k(\xi) \rangle_{\varepsilon_k(\xi)=\varepsilon}$ indicates $X_k(\xi)$ averaged in that region, X_i is $X_k(\xi)$ at the each corner of the pentachoron; w_i can be calculated analytically from $\varepsilon_k(\xi)$ (see Appendix B).

IV. RESULTS

In this section, we show our results of YNi₂B₂C: the normal-state band structure, Fermi surfaces, phonon

TABLE I. Numerical conditions. For the definitions of n_ξ and ε_{min} , see Sec. III B.

k grid (structure and charge density optimization)	$12 \times 12 \times 12$
q grid (wave number of phonons)	$6 \times 6 \times 6$
k grid (density of states)	$40 \times 40 \times 40$
The number of bands (gap equation)	50 bands
The number of bands (polarization function Π_0)	50 bands
The number of points for energy grid n_ξ	100
ε_{min} in energy grid	10^{-6} Ry

dispersion, superconducting transition temperature, gap functions, and quasiparticle DOS in the superconducting phase. We used the DFT code Quantum ESPRESSO [53], which employs plane waves and the pseudopotential to describe the Kohn-Sham orbitals and the crystalline potential, respectively. We obtain phonon frequencies and electron-phonon vertices by using density functional perturbation theory (DFPT) [54]. We employ the optimized tetrahedron method [55,56] for the Brillouin zone integrations in calculations of the charge density, phonons, and the polarization function. We used our open-source program SUPERCONDUCTING TOOLKIT [57] for the calculations concerning SCDFT.

A. Electronic structures of normal state

The calculations were done with the GGA-PBE [58] exchange-correlation functional. We set the plane-wave cutoff for the Kohn-Sham orbitals to 50 Ry. We used the ultrasoft pseudopotentials [59] in Ref. [60]. We also performed the calculations with the LDA-PZ functional [61] and refer to them for comparison when necessary. The numerical conditions are summarized in Table I. We performed calculations with 4^3 , 6^3 , and 8^3 q -point grids and obtained the converged result with the 6^3 grid.

First we performed the structure optimization (crystalline structure is depicted in Fig. 4 (a)); the optimized and experimental structural parameters are given in Table II. The parameter c is underestimated by 2%. Similar underestimation can be seen in a previous report [32], and this is probably due to the drawback with the GGA-PBE functional [32]. The later calculations were based on the theoretically optimized

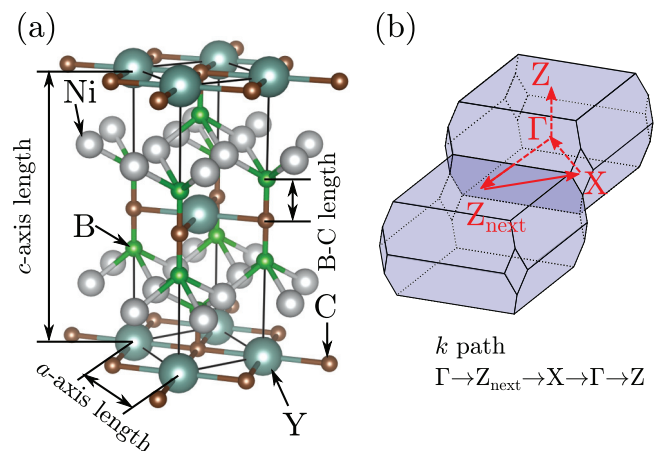


FIG. 4. (a) Crystalline structure of YNi₂B₂C (using VESTA [62]). (b) Brillouin zone and k path.

TABLE II. Results of the structure optimization in comparison with experimental data [63]. Crystal structure is depicted in Fig. 4(a).

	LDA	GGA	Exp.
lattice constant a [Å]	3.48	3.51	3.533
lattice constant c [Å]	10.19	10.31	10.566
B-C length [Å]	1.483	1.494	1.492

lattice parameters, though we have found that the setting of the parameters (either theoretically optimized or experimentally observed values) yields little difference in the calculated phononic and superconducting properties.

Figure 5(a) shows the calculated band structure of $\text{YNi}_2\text{B}_2\text{C}$ [the k path is depicted in Fig. 4(b)]. We here describe the contributions of the atomic orbitals—Y $4d$, Ni $3d$, B $2s2p$, and C $2s2p$ —as the size of the symbols; for example, the Ni $3d$ contribution to the Kohn-Sham state nk $p_{nk}^{\text{Ni}3d}$ is defined by

$$p_{nk}^{\text{Ni}3d} = \sum_{\tau=\text{Ni}1,\text{Ni}2} \sum_m |\langle \varphi_{\tau dm} | \varphi_{nk} \rangle|^2. \quad (25)$$

We also depict the total and the partial density of states in Fig. 5(b). This band structure agrees with the one obtained in the previous study with a GGA functional [64]. There is a flat band near the Fermi level on the X - Γ line; electronic states in this flat band consist mainly of Ni $3d$ state. The total density of states at the Fermi level is 29 states per Ry, spin, and unit cell, to which Y $4d$, Ni $3d$, B $2s2p$, and C $2s2p$ states contribute by 16.5%, 62.7%, 16.6%, and 4.2%, respectively. The large contribution from the Ni $3d$ orbital mainly comes from the proximity of the flat band on the X - Γ line.

Figure 6 shows the Fermi surfaces, on which we describe the distribution of the Fermi velocity with a color plot. It varies largely over Fermi surfaces; the ratio of its maximum to minimum is about 100. We calculate the projections of the atomic orbitals Y $4d$, Ni $3d$, B $2s2p$, and C $2s2s$, to

the electronic states on Fermi surfaces (Fig. 7). There are no regions dominated by B $2s2p$ and C $2s2p$ orbitals. Comparing Figs. 6 and 7, we found that the Fermi velocity is particularly small in the regions where Ni $3d$ orbitals are dominant.

B. Phonons and electron-phonon interactions

We next calculated the phonon and electron-phonon interaction. The calculated frequencies of the Raman-active modes are given in Table III. Results from the previous Raman scattering experiment and first-principles calculation with the all-electron full potential linear augmented plane wave (FLAPW) method and the GGA-PBE functional are also shown. Our results show good agreement with both previous experimental and theoretical results.

We show the calculated phonon dispersions in Fig. 8. The whole spectra agree well with those obtained with the neutron scattering measurement [32] except for the behavior of the TA band around $q \sim 0.55\Gamma Z_{\text{next}}$; although this mode shows strong softening in experiments, the softening obtained in our calculation is not as strong. We observe imaginary modes in the vicinity of the Γ point along the Γ -Z line; this indicates that the system theoretically favors long-period modulation though such a structure has not clearly been observed experimentally. Assuming that the present imaginary modes are an artifact of the present approximation, we just neglect them because phonons with such long wavelength do not affect the superconductivity. We also depict the electron-

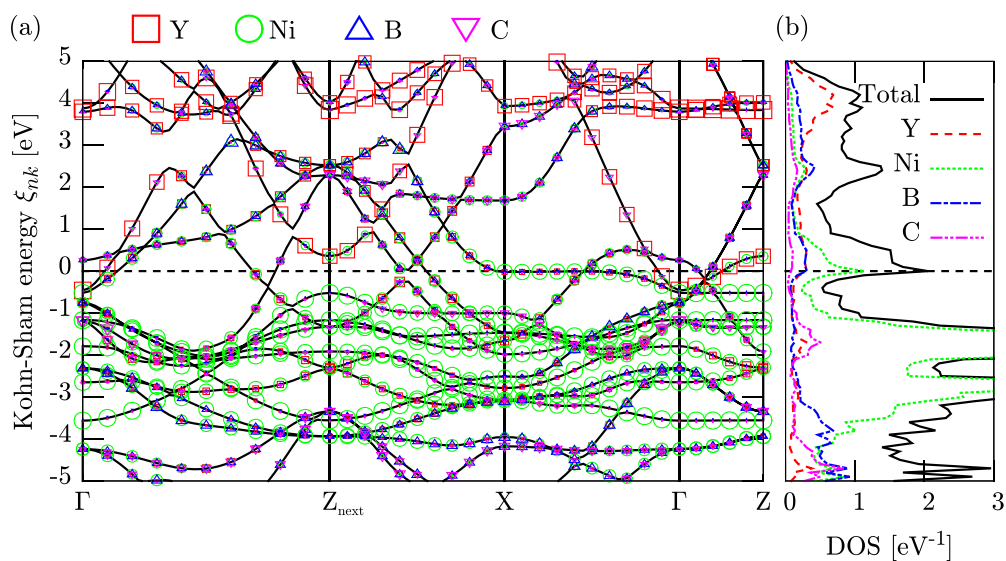


FIG. 5. (a) Band structure of $\text{YNi}_2\text{B}_2\text{C}$. Sizes of red squares, green circles, blue upward triangles, and magenta downward triangles indicate the amount of components of atomic orbitals of Y $4d$, Ni $3d$, B $2s2p$, and C $2s2p$, respectively. (b) Partial and total density of states. The black solid line, the red dashed line, the green dotted line, the blue dashed-dotted line, and the magenta dashed-two dotted line indicate the total Y $4d$, Ni $3d$, B $2s2p$, and C $2s2p$ DOS, respectively.

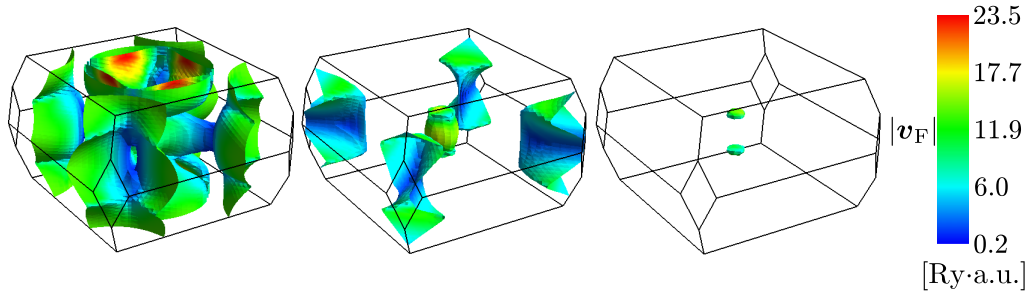


FIG. 6. Fermi velocity of the electronic states on Fermi surfaces. The red, green, and blue region have a high, middle, and low Fermi velocity, respectively. Fermi surfaces in this paper are drawn by using the FermiSurfer [65] program which is developed by us.

phonon coupling constant

$$\lambda_{qv} = \sum_{knn'} \frac{2}{N(\varepsilon_F)\omega_{qv}} |g_{n'k+qnk}^v|^2 \delta(\xi_{nk})\delta(\xi_{n'k+q}) \quad (26)$$

of each phonon (the branch dependent Fröhlich parameter) as radii of circles, where $N(\varepsilon_F)$ is the density of states at the Fermi level; the TA mode has large electron-phonon interaction. The contribution of each atom to each phonon mode can be seen in Fig. 9; there are roughly six groups in this phonon dispersion such as three acoustic branches ranging from 0 meV to 30 meV, Y-dominant branches ranging from 10 meV to 25 meV, Ni-dominant branches ranging from 20 meV to 35 meV, B-C branches ranging from 35 meV to 60 meV, B-dominant branch at approximately 102 meV, and B-C branch at approximately 159 meV. Nondispersive branches at 102 meV and 159 meV have been observed by the time-of-flight neutron spectroscopy experiment [70] in good agreement with our calculation.

The electron-phonon renormalization $Z_{nk} \equiv Z(\{g_{n'k'nk}\}, \{\omega_{k'-k}\}, \xi_{nk})$ of electronic states on the Fermi surfaces are shown in Fig. 10. This has large anisotropy and the ratio between the maximum and the minimum of the Z_{nk} is approximately 4; this ratio is close to the value previously determined with the dHvA experiment [71] referring to the band structure calculation [72]. Comparing Figs. 7 and 10, we can see that the electronic states that have small Z_{nk} consist mainly of Ni 3d orbitals.

From the branch dependent Fröhlich parameter λ_{qv} , we compute the total Fröhlich parameter and the averaged phonon frequency,

$$\lambda = \sum_{qv} \lambda_{qv}, \quad \omega_{ln} = \exp \left[\frac{1}{\lambda} \sum_{qv} \ln(\omega_{qv}) \lambda_{qv} \right]. \quad (27)$$

We obtain $\lambda = 0.72$, and $\omega_{ln} = 270$ K (23.3 meV) by using the GGA-PBE functional; we obtain $\lambda = 0.54$, and $\omega_{ln} =$

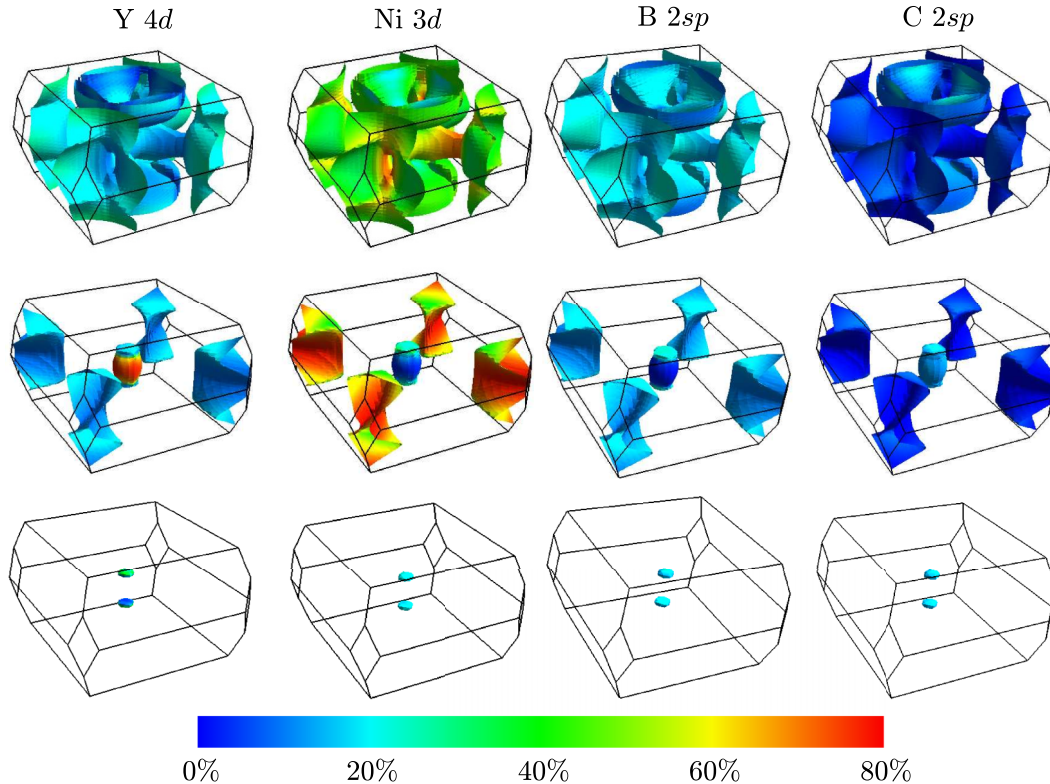


FIG. 7. Projection of atomic orbitals Y 4d, Ni 3d, B 2s2p, and C 2s2s on Fermi surfaces ($|\langle \varphi_{Atom} | \varphi_{nk} \rangle|^2$).

TABLE III. Calculated Raman-active phonon frequencies in cm^{-1} in comparison with those obtained in the previous theoretical work [64] with the full potential linear augmented plane wave (FLAPW) method and the GGA-PBE functional and experimental Raman-scattering measurements.

	This work	Previous (FLAPW) [64]	Previous (experiment)
Ni- B_{1g}	193	200	199 [66], 198 [67], 193 [68]
Ni- E_g	279	271	287 [66], 282 [67]
B- E_g	461	447	460 [66], 470 [67]
B- A_{1g}	836	821	813 [66], 832 [67], 823 [68], 847 [69]

291 K (25.1 meV) by using the LDA-PZ functional. We can find the origin of the functional dependence of the phonon dispersion and the Fröhlich parameter follows. Figure 11 shows phonon dispersions and Eliashberg functions computed in three different conditions, namely, the GGA functional with the GGA geometry (a geometry optimized with the GGA functional), the LDA functional with the LDA geometry, and the GGA functional with the LDA geometry. When we use the LDA geometry, the phonon is hardened because of the underestimated interatomic distance. From this hardened phonon, we obtain a small λ . This overestimation of the phonon frequency is improved by using the GGA geometry. We see below that this dependence on the exchange-correlation functional yields some variation of the resulting T_c , though the superconducting solution is robustly present. The Fröhlich parameter computed with the GGA functional is slightly smaller than that from the specific heat measurement $\lambda_{S-H} = \gamma_{\text{exp}}/\gamma_{\text{band}} - 1 = 0.82$, where $\gamma_{\text{exp}} = 18.2 \text{ mJ/mol/K}^2$ is the Sommerfeld parameter from the specific heat measurement [73] and $\gamma_{\text{band}} = 10.0 \text{ mJ/mol/K}^2$ is that parameter obtained from the band structure computed in the current work. This underestimation probably comes from the incomplete reproduction of the

phonon softening of the TA band around $q \sim 0.55\Gamma Z_{\text{next}}$ (see Fig. 8).

C. Superconducting gaps and transition temperature

Let us now move on to the superconducting properties. We calculated the superconducting gap function at various temperatures. The values of the gap function averaged over the Fermi surfaces for the respective temperatures, as well as the maximum and minimum values are plotted in Fig. 12. The calculated transition temperature where superconducting gaps disappear, 13.8 K, agrees well with the experimental value, 15.4 K. We also obtained the superconducting solution with the LDA-PZ functional; although the resulting T_c is 8.73 K, this result indicates that the superconducting phase is numerically robust against the change of the exchange-correlation functional. The calculated isotope effect exponent for boron atoms α_B is 0.16, in fair agreement with the experimentally observed values ($\alpha_B = 0.11 \pm 0.05$, 0.21 ± 0.07 [31], 0.25 ± 0.04 , 0.27 ± 0.07 , 0.26 ± 0.03 [30]).

We depict the superconducting gap function Δ_{nk} on Fermi surfaces at low temperature (0.1 K) in Fig. 13 [74]. As we

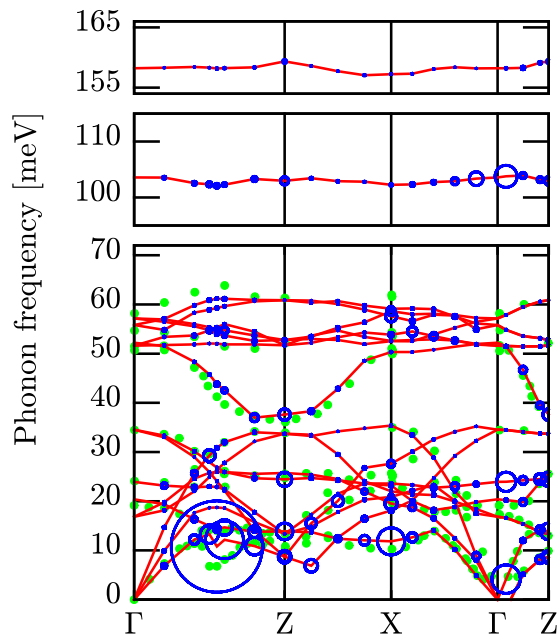


FIG. 8. Phonon dispersion. The radii of circles indicate magnitude of λ_{qv} . Green filled circles indicate results of the neutron diffraction [32].

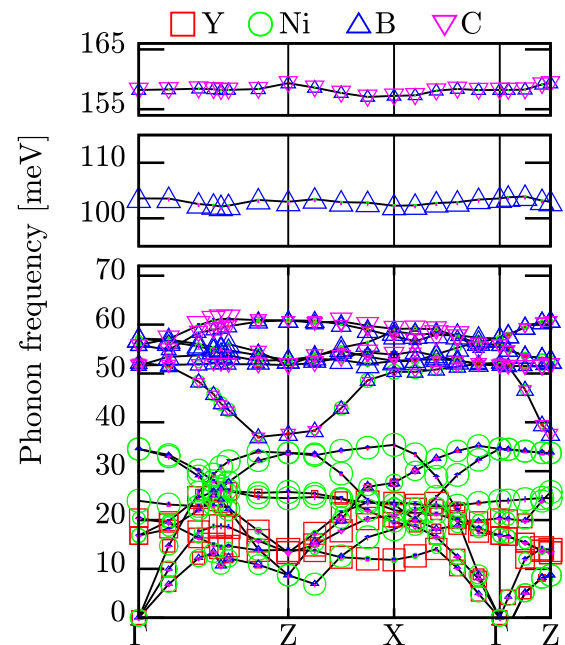
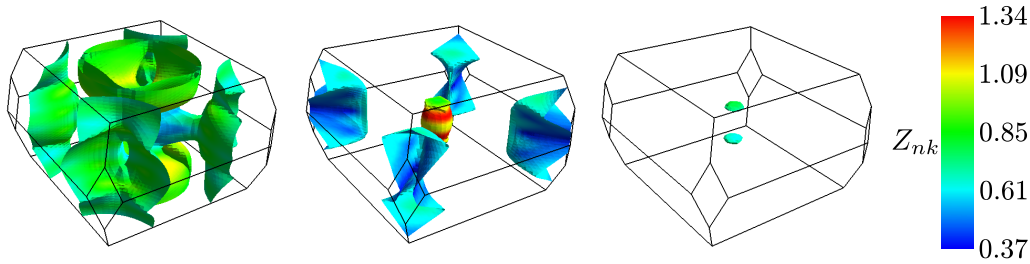


FIG. 9. Phonon dispersion. Sizes of red squares, green circles, blue upward triangles, and magenta downward triangles indicate magnitude of components of Y, Ni, B, and C, respectively, of the displacement pattern.

FIG. 10. Electron-phonon renormalization Z_{nk} on Fermi surfaces.

expected, superconducting gaps of YNi₂B₂C are anisotropic; similar to the case of Z_{nk} , electronic states that have a small superconducting gap consist of Ni 3d orbitals. However, the degree of anisotropy is smaller than that of the electron-phonon coupling; the ratio between the maximum and minimum of the gap functions on Fermi surfaces is 2.4. This suppression of anisotropy comes from the following two reasons: First, the nk dependence of the screened Coulomb interaction cancels the nk -dependent pairing induced by the phonon. Figure 14 shows the nk dependent Coulomb potential

$$\mu_{nk} \equiv \sum_{qn'} \delta(\xi_{n'k+q}) K^{ec} [V_{n'k+qnk}] (\xi_{nk}, \xi_{n'k+q}). \quad (28)$$

The sign of the Coulomb repulsion and the phonon mediated attraction is opposite, while their absolute values are positively correlated. The dependence of their sum is thus moderated. Second, the integration kernel in Eq. (2) is reduced by a factor $1/(1 + Z_{nk})$; this renormalization is large in the region where

the electron-phonon interaction is strong. Consequently, the anisotropy of the integration kernel becomes smaller than that of the electron-phonon interaction, and the anisotropy of the superconducting gap is suppressed.

To examine the effect of the exchange-correlation kernel $\delta^2 E_{XC}/\delta^2 \rho$ in the electron-electron kernel [Eq. (6)], we calculate superconducting gap by using RPA also; the difference in the T_c was less than 0.1 K compared with that from the ALDA. Therefore, in YNi₂B₂C, the effect of the exchange-correlation kernel is very small at the ALDA level. We perform a converse calculation of the Coulomb pseudopotential μ^* , which is usually treated as a fitting parameter for McMillan's formula [75,76]

$$T_c = \frac{\omega_{in}}{1.2} \exp\left(\frac{-1.04(1 + \lambda)}{\lambda - \mu^*(1 + 0.62\lambda)}\right). \quad (29)$$

Namely, we determined μ^* so that the transition temperatures calculated with the RPA-SCDFT and ALDA-SCDFT are reproduced with $\lambda = 0.72$ and $\omega_{in} = 267$ K; We obtain $\mu^* = 0.053$ in both cases. Notably, this value is far smaller than the conventional range (0.10–0.13 [77]). This indicates that the nk -averaging approximation, which is applicable to ordinary materials, substantially underestimate T_c and the anisotropy is important for the observed high T_c .

Using the calculated k -dependent gap function, we next evaluated the quasiparticle density of states (QPDOS) in the superconducting phase. The calculated QPDOS is compared

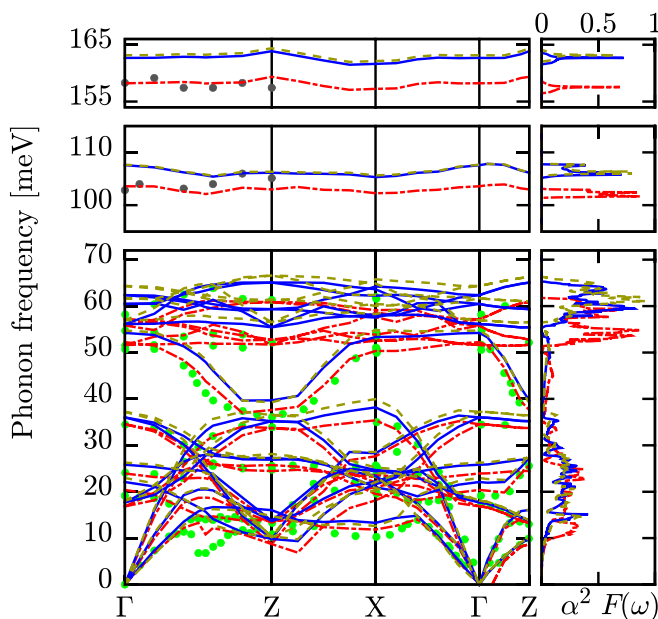


FIG. 11. Phonon dispersions and Eliashberg functions computed in three different conditions. The red dashed-dotted line, the blue solid line, and the yellow dashed line indicate those computed by using the GGA functional with the GGA geometry (a geometry optimized with the GGA functional), the LDA functional with the LDA geometry, and the GGA functional with the LDA geometry, respectively. Green and gray filled circles indicate results of the neutron diffraction experiment in Refs. [32,70], respectively.

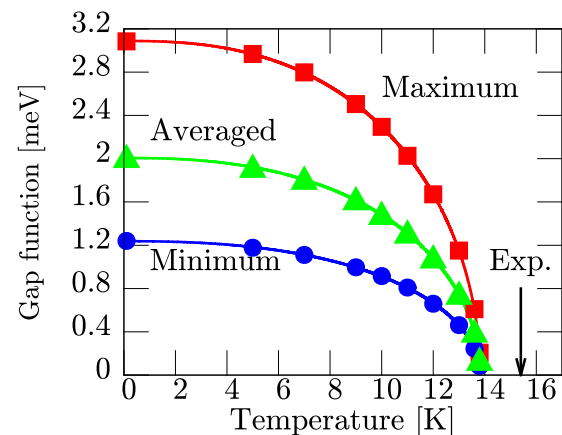
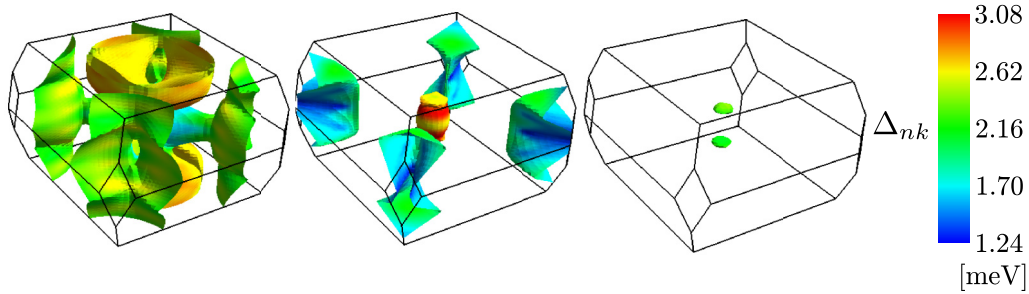


FIG. 12. Calculated and experimental superconducting transition temperature. Red squares, green triangles, and blue circles indicate the maximum, the averaged, and the minimum superconducting gaps on Fermi surfaces; solid lines are a fit of these gaps with a function $\Delta(T) = \Delta_0 \{1 - (T/T_c)^p\}^{1/q}$ via Δ_0, T_c, p , and q .

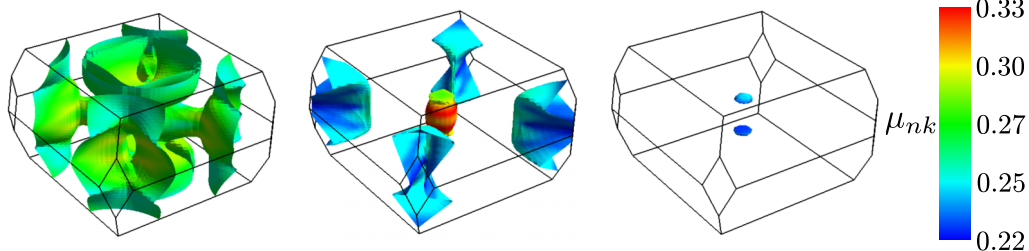
FIG. 13. Superconducting gap functions Δ_{nk} on Fermi surfaces at 0.1 K.

to the density of states extracted from the tunnel-conductance measurement [11] (Fig. 15); although there is a visible discrepancy between the peak positions of the calculated QPDOS and the experimental spectrum, their whole shapes are very similar (Fig. 12). Note that we did not use the smearing method for the four-dimensional integral; therefore, the broadened peak structure definitely originates from the k -space variation of the gap function. If we use the smearing, we cannot distinguish a broadened peak made by the variation of the gap function and one made by the smearing.

V. DISCUSSION

As revealed with Fig. 13, the k -space distribution shows full s -wave gap with subtle dependence which is obviously composed of multiple high order spherical harmonics. As a result, Δ_{nk} shows continuous spectrum across the multiple Fermi surfaces; namely, multiband extended s -wave gap. Here we note that the superconducting gap has significant intraband anisotropy; this is in stark contrast with the “anisotropic gap” in MgB_2 , where the gap value varies with bands but does not vary much within each Fermi surface [78]. We have found a significant correlation between the anisotropy of the superconducting gaps in $\text{YNi}_2\text{B}_2\text{C}$ and the variation of the ratio of atomic orbitals on the Fermi surfaces. The electronic states on the Fermi surfaces in $\text{YNi}_2\text{B}_2\text{C}$ consist of Y $4d$, Ni $3d$, B $2s2p$, and C $2s2p$; in particular, the electronic states dominated by Ni $3d$ orbitals couple to phonons very weakly, consequently exhibiting very small gap. To evaluate contributions from each atomic orbital to the superconducting gap, we defined the superconducting gaps of each orbital Δ_o ($o = Y4d, Ni3d, B2s2p$, and $C2s2p$) as the fitting parameters of Δ_{nk} in the following form:

$$\Delta_{nk}^{\text{test}} = \Delta_{Y4d} p_{nk}^{Y4d} + \Delta_{Ni3d} p_{nk}^{Ni3d} + \Delta_{B2s2p} p_{nk}^{B4d} + \Delta_{C2s2p} p_{nk}^{C2s2p}. \quad (30)$$

FIG. 14. The nk dependent Coulomb potential defined in Eq. (28).

The factors p_{nk} s are contributions of the respective atomic orbitals to the electronic state φ_{nk} [Eq. (25)]. We determined Δ_{Y4d} , Δ_{Ni3d} , Δ_{B2s2p} , and Δ_{C2s2p} so that the following variance is minimized

$$\sigma^2 = \sum_{nk} \delta(\xi_{nk}) (\Delta_{nk} - \Delta_{nk}^{\text{test}})^2; \quad (31)$$

we obtained $\Delta_{Y4d} = 2.0$, $\Delta_{Ni3d} = 1.5$, $\Delta_{B2s2p} = 3.9$, and $\Delta_{C2s2p} = 10.8$, with the fitting error

$$\left\langle \frac{\delta\Delta}{\Delta} \right\rangle = \frac{\sum_{nk} \delta(\xi_{nk}) |\Delta_{nk} - \Delta_{nk}^{\text{test}}| / |\Delta_{nk}|}{\sum_{nk} \delta(\xi_{nk})} \quad (32)$$

being 12.6 %. We also applied a similar analysis on the electron-phonon renormalization Z_{nk} : Namely, we fit the electron-phonon renormalization Z_{nk} into the orbital-dependent form

$$Z_{nk}^{\text{test}} = Z_{Y4d} p_{nk}^{Y4d} + Z_{Ni3d} p_{nk}^{Ni3d} + Z_{B2s2p} p_{nk}^{B4d} + Z_{C2s2p} p_{nk}^{C2s2p}. \quad (33)$$

We obtain $Z_{Y4d} = 0.85$, $Z_{Ni3d} = 0.45$, $Z_{B2s2p} = 1.21$, and $Z_{C2s2p} = 4.22$, with the fitting error $\langle \delta Z / Z \rangle = 14.9$. The small value of Z_{Ni3d} indicates that the mixing of Ni $3d$ orbitals weakens the interaction with the phonons, which is the key factor behind the mechanism of the anisotropic gap.

The relatively accurate fitting errors in the above analysis suggest that, in the real space, the coupling to phonons and gaps at the respective atoms possibly exhibit specific values. The gap structure varying within the respective Fermi-surface sheets is then interpreted to originate from the complicated hybridization between the atomic orbitals. A recently developed real-space method [79] could be helpful to substantiate this scenario.

Here we discuss why the Ni $3d$ orbital results in the weak electron-phonon interaction. We infer that the localized nature of Ni $3d$ orbitals has a crucial role; this localization

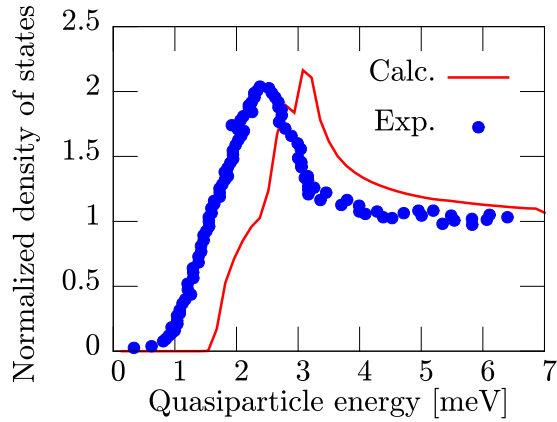


FIG. 15. Calculated superconducting quasiparticle density of states at 0.1 K and experimental tunnel conductance spectrum at 0.5 K [11].

affects the screened electron-phonon interaction through the following two possible routes: It makes the electronic states more sensitive to the deformation potential of the Ni ion, which should yield stronger electron-phonon coupling. On the other hand, the highly localized Ni 3d electrons participate in the local screening of the deformation potential, which should make the electron-phonon coupling weak. In the present case, the latter is considered to be dominant. To confirm this point, we calculate the renormalization factor Z_{nk} by using the bare electron-phonon vertex (note that the electron-phonon vertex employed for the superconducting calculations are usually calculated with the screened perturbation potential of atomic displacements). Figure 16 shows the resulting Z_{bare} : Performing the same fitting as before, we obtain $Z_{Y4d} = 6.3 \times 10^3$, $Z_{\text{Ni}3d} = 3.8 \times 10^4$, $Z_{\text{B}2s2p} = -1.3 \times 10^4$, and $Z_{\text{C}2s2p} = 6.7 \times 10^3$; the fitting error is 39.1% [80]. $Z_{\text{Ni}3}$ is larger than other Z s when we use the bare vertex whereas it is smaller than the others when we use the screened vertex. This result shows that the screening effect on the interaction between the Ni 3d orbital and phonons is particularly large; this strong screening makes the interaction especially weak. There is also some supporting experimental evidence of our scenario. First, $\text{YPd}_2\text{B}_2\text{C}$ has the transition temperature higher than that of $\text{YNi}_2\text{B}_2\text{C}$ [81]. Second, the anomalous behavior of the specific heat of $\text{YNi}_2\text{B}_2\text{C}$ is reduced when some Ni atoms are replaced with Pt atoms in the specific-heat measurement [8–10]. According to our scenario, the Pd 4d orbitals and Pt 5d orbitals are more delocalized than the Ni 3d orbitals, and this delocalized nature is advantageous to the electron-phonon coupling. We reproduced quantitatively the

superconducting T_c , the isotope effect constant, the phonon dispersion excepting the large softening of the TA mode and reproduced qualitatively by the broadened peak structure in the tunnel conductance [11], and the k dependence of Δ_{nk} observed by ARPES [14]. However, the anisotropy of the superconducting gap in our calculation is too small to reproduce the ultrasonic attenuation measurement [12] and the magnetic field dependence of the thermal conductivity [13]. We assume one of the origin of this underestimation of the anisotropy to be in the calculation of the electronic structure in the normal state. In the previous study of the combination of dHvA experiment [71] and the band-structure calculation [72], authors shifted upwardly Y 4d and Ni 3d levels from the LDA levels by 0.11 Ry and 0.05 Ry. They state these shifts correspond to the self-interaction and/or the nonlocal correction to the LDA. On the other hand, reproduction of the Fermi surfaces that agree well with the experiments without such an empirical treatment has not been achieved so far. Thus, the detailed shape of the Fermi surfaces has not been settled. If we improve on the description of the Fermi surface, the following may be accomplished.

(1) The nesting which corresponds to the TA mode at $q = 0.55\Gamma Z_{\text{next}}$ becomes more significant, yielding stronger softening of the low-energy phonon mode; the strength of the nesting is sensitive to the fine structure of the Fermi surface.

(2) Regions which consist *only* of Ni 3d orbital appear; such regions should couple with phonons very weakly and have quite small gaps.

VI. SUMMARY

In this study, we performed a first principle investigation to clarify the origin of the anisotropic superconductivity in $\text{YNi}_2\text{B}_2\text{C}$. We improved the numerical method for the k integration in the gap equation to treat accurately k dependencies of the electron-phonon interaction and the gap function. From calculations with this method, we found that the anisotropic superconductivity is traced back to the variation of the rate of the Ni 3d orbital on the Fermi surface. As the component of the Ni 3d orbital increases, the electron-phonon coupling of the electronic state becomes weak and its superconducting gap function becomes small. Because of this effect, the superconducting gap significantly varying over the Fermi surface emerges. As a possible scenario, we proposed that the localized nature of the Ni 3d orbitals is a key factor for the weakening of the electron-phonon coupling. We found the relation between the peculiar electron-phonon interaction and the electronic state in the vicinity of the Fermi surface in this material.

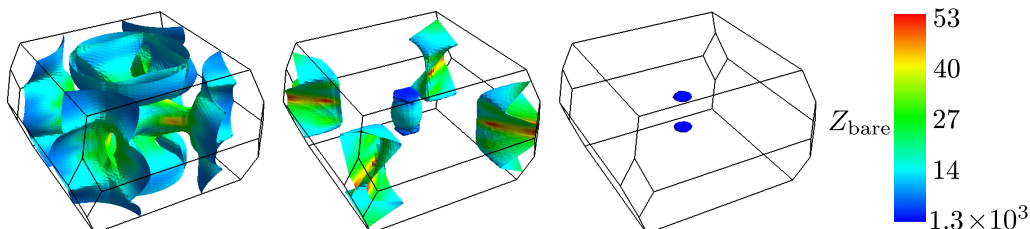


FIG. 16. The electron-phonon renormalization Z calculated by using the bare electron-phonon vertex on Fermi surfaces.

ACKNOWLEDGMENTS

We thank Yasutami Takada for his invaluable advice. This work was supported by the MEXT Element Strategy Initiative to Form Core Research Center. The numerical calculations were performed using Fujitsu FX10s at the Information Technology Center and the Institute for Solid State Physics, The University of Tokyo.

APPENDIX A: FREQUENCY INTEGRATION IN EQ. (4)

In Eq. (4), we perform an integration from 0 to the infinity as follows: First we employ a new variable x , where

$$\omega = (|\xi_{nk}| + |\xi_{n'k'}|) \frac{1+x}{1-x}, \quad (\text{A1})$$

and we obtain

$$K^{\text{ee}}[V_{n'k'nk}](\xi_{nk}, \xi_{n'k'}) = \frac{2}{\pi} \int_{-1}^1 dx \frac{1}{1+x^2} V_{nkn'k'} \times \left((|\xi_{nk}| + |\xi_{n'k'}|) \frac{1+x}{1-x} \right). \quad (\text{A2})$$

We use the Gauss-Legendre quadrature for this integration. To obtain the Coulomb interaction $V_{nkn'k'}(\omega)$ at an arbitrary frequency ω , we employ the Chebyshev interpolation [82].

APPENDIX B: FOUR-DIMENSIONAL NUMERICAL INTEGRATION SCHEME FOR DOS

We calculate the integration weight w_i in Eq. (24) as follows, where $f_{ij} \equiv (\varepsilon - \varepsilon_j)/(\varepsilon_i - \varepsilon_j)$, ε_i is $\varepsilon_k(\xi)$ at the each corner of a pentachoron.

(1) For $\varepsilon_1 < \varepsilon < \varepsilon_2 < \varepsilon_3 < \varepsilon_4 < \varepsilon_5$, we obtain

$$C = \frac{f_{21} f_{31} f_{41}}{\varepsilon_5 - \varepsilon_1} \quad (\text{B1})$$

$$w_1 = C(f_{12} + f_{13} + f_{14} + f_{15}),$$

$$w_2 = C f_{21}, \quad w_3 = C f_{31},$$

$$w_4 = C f_{41}, \quad w_5 = C f_{51}. \quad (\text{B2})$$

(2) For $\varepsilon_1 < \varepsilon_2 < \varepsilon < \varepsilon_3 < \varepsilon_4 < \varepsilon_5$, we obtain

$$C_1 = \frac{f_{31} f_{41} f_{23}}{\varepsilon_5 - \varepsilon_1}, \quad C_2 = \frac{f_{41} f_{32} f_{24}}{\varepsilon_5 - \varepsilon_1}, \quad C_3 = \frac{f_{32} f_{42} f_{25}}{\varepsilon_5 - \varepsilon_1} \quad (\text{B3})$$

$$w_1 = C_1(f_{13} + f_{14} + f_{15}) + C_2(f_{14} + f_{15}) + C_3 f_{15},$$

$$w_2 = C_1 f_{23} + C_2(f_{23} + f_{24}) + C_3(f_{23} + f_{24} + f_{25}),$$

$$w_3 = C_1(f_{31} + f_{32}) + C_2 f_{32} + C_3 f_{32},$$

$$w_4 = C_1 f_{41} + C_2(f_{41} + f_{42}) + C_3 f_{42},$$

$$w_5 = C_1 f_{51} + C_2 f_{51} + C_3(f_{51} + f_{52}). \quad (\text{B4})$$

(3) For $\varepsilon_1 < \varepsilon_2 < \varepsilon_3 < \varepsilon < \varepsilon_4 < \varepsilon_5$, we obtain

$$C_1 = \frac{f_{35} f_{25} f_{43}}{\varepsilon_5 - \varepsilon_1}, \quad C_2 = \frac{f_{25} f_{34} f_{42}}{\varepsilon_5 - \varepsilon_1}, \quad C_3 = \frac{f_{34} f_{24} f_{41}}{\varepsilon_5 - \varepsilon_1} \quad (\text{B5})$$

$$w_1 = C_1 f_{15} + C_2 f_{15} + C_3(f_{14} + f_{15}),$$

$$w_2 = C_1 f_{25} + C_2(f_{24} + f_{25}) + C_3 f_{24},$$

$$w_3 = C_1(f_{34} + f_{35}) + C_2 f_{34} + C_3 f_{34},$$

$$w_4 = C_1 f_{43} + C_2(f_{42} + f_{43}) + C_3(f_{41} + f_{42} + f_{43}),$$

$$w_5 = C_1(f_{53} + f_{52} + f_{51}) + C_2(f_{51} + f_{52}) + C_3 f_{51}. \quad (\text{B6})$$

(4) For $\varepsilon_1 < \varepsilon_2 < \varepsilon_3 < \varepsilon_4 < \varepsilon < \varepsilon_5$, we obtain

$$C = \frac{f_{45} f_{35} f_{25}}{\varepsilon_5 - \varepsilon_1} \quad (\text{B7})$$

$$w_1 = C f_{15}, \quad w_2 = C f_{25},$$

$$w_3 = C f_{35}, \quad w_4 = C f_{45},$$

$$w_5 = C(f_{51} + f_{52} + f_{53} + f_{54}). \quad (\text{B8})$$

-
- [1] J. Bardeen, L. N. Cooper, and J. R. Schrieffer, *Phys. Rev.* **108**, 1175 (1957).
- [2] G. M. Eliashberg, *Zh. Eksp. Teor. Fiz.* **38**, 966 (1960) [*Sov. Phys. JETP-USSR* **11**, 696 (1960)].
- [3] N. Plakida, *High-Temperature Cuprate Superconductors: Experiment, Theory, and Applications*, Springer Series in Solid-State Sciences, Vol. 166 (Springer, Berlin, Heidelberg, 2010), pp. 1–570.
- [4] G. R. Stewart, *Rev. Mod. Phys.* **83**, 1589 (2011).
- [5] C. Pfleiderer, *Rev. Mod. Phys.* **81**, 1551 (2009).
- [6] C. Mazumdar, R. Nagarajan, C. Godart, L. Gupta, M. Latroche, S. Dhar, C. Levy-Clement, B. Padalia, and R. Vijayaraghavan, *Solid State Commun.* **87**, 413 (1993).
- [7] R. Cava, H. Takagi, H. Zandbergen, J. Krajewski, W. Peck, T. Siegrist, B. Batlogg, R. Vandover, R. Felder, K. Mizuhashi, J. Lee, H. Eisaki, and S. Uchida, *Nature(London)* **367**, 252 (1994).
- [8] M. Nohara, M. Isshiki, F. Sakai, and H. Takagi, *J. Phys. Soc. Jpn.* **68**, 1078 (1999).
- [9] M. Nohara, H. Suzuki, N. Mangkorntong, and H. Takagi, *Physica C* **341-348**, 2177 (2000).
- [10] K. Izawa, A. Shibata, Y. Matsuda, Y. Kato, H. Takeya, K. Hirata, C. J. van der Beek, and M. Konczykowski, *Phys. Rev. Lett.* **86**, 1327 (2001).
- [11] P. Martínez-Samper, H. Suderow, S. Vieira, J. P. Brison, N. Luchier, P. Lejay, and P. C. Canfield, *Phys. Rev. B* **67**, 014526 (2003).
- [12] T. Watanabe, M. Nohara, T. Hanaguri, and H. Takagi, *Phys. Rev. Lett.* **92**, 147002 (2004).
- [13] K. Izawa, K. Kamata, Y. Nakajima, Y. Matsuda, T. Watanabe, M. Nohara, H. Takagi, P. Thalmeier, and K. Maki, *Phys. Rev. Lett.* **89**, 137006 (2002).
- [14] T. Baba, T. Yokoya, S. Tsuda, T. Watanabe, M. Nohara, H. Takagi, T. Oguchi, and S. Shin, *Phys. Rev. B* **81**, 180509 (2010).
- [15] T. Kohara, T. Oda, K. Ueda, Y. Yamada, A. Mahajan, K. Elankumaran, Z. Hossian, L. C. Gupta, R. Nagarajan, R. Vijayaraghavan, and C. Mazumdar, *Phys. Rev. B* **51**, 3985 (1995).

- [16] Z. Hossain, S. K. Dhar, R. Nagarajan, L. C. Gupta, C. Godart, and R. Vijayaraghavan, *IEEE Trans. Magn.* **31**, 4133 (1995).
- [17] R. Nagarajan, L. Gupta, C. Mazumdar, Z. Hossain, S. Dhar, C. Godart, B. Padalia, and R. Vijayaraghavan, *J. Alloys Compd.* **225**, 571 (1995).
- [18] K. Prassides, A. Lappas, M. Buchgeister, and P. Verges, *Europhys. Lett.* **29**, 641 (1995).
- [19] P. Canfield, B. Cho, and K. Dennis, *Physica B* **215**, 337 (1995).
- [20] B. K. Cho, P. C. Canfield, and D. C. Johnston, *Phys. Rev. B* **53**, 8499 (1996).
- [21] B. K. Cho, P. C. Canfield, and D. C. Johnston, *Phys. Rev. B* **52**, R3844(R) (1995).
- [22] A. I. Goldman, C. Stassis, P. C. Canfield, J. Zarestky, P. Dervenagas, B. K. Cho, D. C. Johnston, and B. Sternlieb, *Phys. Rev. B* **50**, 9668(R) (1994).
- [23] J. Zarestky, C. Stassis, A. I. Goldman, P. C. Canfield, P. Dervenagas, B. K. Cho, and D. C. Johnston, *Phys. Rev. B* **51**, 678 (1995).
- [24] B. K. Cho, M. Xu, P. C. Canfield, L. L. Miller, and D. C. Johnston, *Phys. Rev. B* **52**, 3676 (1995).
- [25] Z. Zeng, D. Guenzburger, D. Ellis, and E. Baggio-Saitovitch, *Physica C: Superconductivity* **271**, 23 (1996).
- [26] A. O. Shorikov, V. I. Anisimov, and M. Sigrist, *J. Phys.: Condens. Matter* **18**, 5973 (2006).
- [27] M. A. Ruderman and C. Kittel, *Phys. Rev.* **96**, 99 (1954).
- [28] T. Kasuya, *Prog. Theor. Phys.* **16**, 45 (1956).
- [29] K. Yosida, *Phys. Rev.* **106**, 893 (1957).
- [30] D. Lawrie and J. Franck, *Physica C* **245**, 159 (1995).
- [31] K. Cheon, I. Fisher, and P. Canfield, *Physica C* **312**, 35 (1999).
- [32] F. Weber, L. Pintschovius, W. Reichardt, R. Heid, K.-P. Bohnen, A. Kreyssig, D. Reznik, and K. Hradil, *Phys. Rev. B* **89**, 104503 (2014).
- [33] P. B. Allen and B. Mitrovic in *Solid State Physics*, edited by H. Ehrenreich, F. Seitz, and D. Turnbull (Academic, New York, 1982), Vol. 37, p. 1.
- [34] J. Nagamatsu, N. Nakagawa, T. Muranaka, Y. Zenitani, and J. Akimitsu, *Nature (London)* **410**, 63 (2001).
- [35] H. Choi, D. Roundy, H. Sun, M. Cohen, and S. Louie, *Nature (London)* **418**, 758 (2002).
- [36] H. Kamimura, S. Matsuno, Y. Suwa, and H. Ushio, *Phys. Rev. Lett.* **77**, 723 (1996).
- [37] L. N. Oliveira, E. K. U. Gross, and W. Kohn, *Phys. Rev. Lett.* **60**, 2430 (1988).
- [38] M. Lüders, M. A. L. Marques, N. N. Lathiotakis, A. Floris, G. Profeta, L. Fast, A. Continenza, S. Massidda, and E. K. U. Gross, *Phys. Rev. B* **72**, 024545 (2005).
- [39] E. R. Margine and F. Giustino, *Phys. Rev. B* **87**, 024505 (2013).
- [40] A. Sanna, G. Profeta, A. Floris, A. Marini, E. K. U. Gross, and S. Massidda, *Phys. Rev. B* **75**, 020511 (2007).
- [41] M. A. L. Marques, M. Lüders, N. N. Lathiotakis, G. Profeta, A. Floris, L. Fast, A. Continenza, E. K. U. Gross, and S. Massidda, *Phys. Rev. B* **72**, 024546 (2005).
- [42] G. Profeta, C. Franchini, N. N. Lathiotakis, A. Floris, A. Sanna, M. A. L. Marques, M. Lüders, S. Massidda, E. K. U. Gross, and A. Continenza, *Phys. Rev. Lett.* **96**, 047003 (2006).
- [43] R. Akashi and R. Arita, *Phys. Rev. Lett.* **111**, 057006 (2013).
- [44] A. Zangwill and P. Soven, *Phys. Rev. A* **21**, 1561 (1980).
- [45] D. A. Kirzhnits, E. G. Maksimov, and D. I. Khomskii, *J. Low Temp. Phys.* **10**, 79 (1973).
- [46] Y. Takada, *J. Phys. Soc. Jpn.* **45**, 786 (1978).
- [47] Y. Nambu, *Phys. Rev.* **117**, 648 (1960).
- [48] L. Gor'kov, *Sov. Phys. JETP* **7**, 505 (1958).
- [49] A. Floris, G. Profeta, N. N. Lathiotakis, M. Lüders, M. A. L. Marques, C. Franchini, E. K. U. Gross, A. Continenza, and S. Massidda, *Phys. Rev. Lett.* **94**, 037004 (2005).
- [50] J. Schrieffer, *Theory of Superconductivity*, Advanced Book Program Series (Perseus Books, New York, 1983).
- [51] Y. Takada, *J. Phys. Soc. Jpn.* **49**, 1267 (1980).
- [52] O. Jepsen and O. K. Andersen, *Solid State Commun.* **9**, 1763 (1971).
- [53] P. Giannozzi, S. Baroni, N. Bonini, M. Calandra, R. Car, C. Cavazzoni, D. Ceresoli, G. L. Chiarotti, M. Cococcioni, I. Dabo, A. Dal Corso, S. de Gironcoli, S. Fabris, G. Fratesi, R. Gebauer, U. Gerstmann, C. Gougoussis, A. Kokalj, M. Lazzeri, L. Martin-Samos, N. Marzari, F. Mauri, R. Mazzarello, S. Paolini, A. Pasquarello, L. Paulatto, C. Sbraccia, S. Scandolo, G. Sclauzero, A. P. Seitsonen, A. Smogunov, P. Umari, and R. M. Wentzcovitch, *J. Phys.: Condens. Matter* **21**, 395502 (2009).
- [54] S. Baroni, S. de Gironcoli, A. Dal Corso, and P. Giannozzi, *Rev. Mod. Phys.* **73**, 515 (2001).
- [55] M. Kawamura, Y. Gohda, and S. Tsuneyuki, *Phys. Rev. B* **89**, 094515 (2014).
- [56] We release a patch to the Quantum ESPRESSO for using the tetrahedron method in the calculation of phonons, <http://qe-forge.org/gf/project/dfpttetra/frs/>. We develop also a library for implementing the optimized tetrahedron method in an arbitrary program, <http://libtetrazb.osdn.jp/>.
- [57] <http://sctk.osdn.jp/>.
- [58] J. P. Perdew, K. Burke, and M. Ernzerhof, *Phys. Rev. Lett.* **78**, 1396 (1997).
- [59] D. Vanderbilt, *Phys. Rev. B* **41**, 7892 (1990).
- [60] We use the pseudopotentials Y.pbe-spn-rrkjus_psl.0.2.3.UPF, Ni.pbe-n-rrkjus_psl.0.1.UPF, B.pbe-n-rrkjus_psl.0.1.UPF, and C.pbe-n-rrkjus_psl.0.1.UPF in PSLibrary 0.3.1, <http://theosrv1.epfl.ch/Main/Pseudopotentials>.
- [61] J. P. Perdew and A. Zunger, *Phys. Rev. B* **23**, 5048 (1981).
- [62] K. Momma and F. Izumi, *J. Appl. Cryst.* **44**, 1272 (2011).
- [63] T. Siegrist, R. Cava, J. Krajewski, and W. F. Peck, Jr., *J. Alloys Compd.* **216**, 135 (1994).
- [64] P. Ravindran, A. Kjekshus, H. Fjellvåg, P. Puschnig, C. Ambrosch-Draxl, L. Nordström, and B. Johansson, *Phys. Rev. B* **67**, 104507 (2003).
- [65] <http://fermisurfer.osdn.jp/>.
- [66] J. Hartmann, F. Gompf, and B. Renker, *J. Low Temp. Phys.* **105**, 1629 (1996).
- [67] V. G. Hadjiev, L. N. Bozukov, and M. G. Baychev, *Phys. Rev. B* **50**, 16726 (1994).
- [68] H.-J. Park, H.-S. Shin, H.-G. Lee, I.-S. Yang, W. C. Lee, B. K. Cho, P. C. Canfield, and D. C. Johnston, *Phys. Rev. B* **53**, 2237 (1996).
- [69] A. P. Litvinchuk, L. Börjesson, N. X. Phuc, and N. M. Hong, *Phys. Rev. B* **52**, 6208 (1995).
- [70] F. Weber, S. Rosenkranz, L. Pintschovius, J.-P. Castellan, R. Osborn, W. Reichardt, R. Heid, K.-P. Bohnen, E. A. Goremychkin, A. Kreyssig, K. Hradil, and D. L. Abernathy, *Phys. Rev. Lett.* **109**, 057001 (2012).
- [71] T. Terashima, H. Takeya, S. Uji, K. Kadowaki, and H. Aoki, *Solid State Commun.* **96**, 459 (1995).
- [72] K. Yamauchi, H. Katayama-Yoshida, A. Yanase, and H. Harima, *Physica C* **412-414**, 225 (2004).

- [73] H. Michor, T. Holubar, C. Dusek, and G. Hilscher, *Phys. Rev. B* **52**, 16165 (1995).
- [74] Calculation at 0 K needs special treatment, and the result at 0 K and that at 0.1 K are almost the same; therefore we calculate at 0.1 K instead of 0 K.
- [75] W. L. McMillan, *Phys. Rev.* **167**, 331 (1968).
- [76] R. Dynes, *Solid State Commun.* **10**, 615 (1972).
- [77] P. Morel and P. W. Anderson, *Phys. Rev.* **125**, 1263 (1962).
- [78] H. J. Choi, D. Roundy, H. Sun, M. L. Cohen, and S. G. Louie, *Phys. Rev. B* **66**, 020513 (2002).
- [79] A. Linscheid, A. Sanna, A. Floris, and E. K. U. Gross, *Phys. Rev. Lett.* **115**, 097002 (2015).
- [80] The cause of the increase in fitting error is that the bare deformation potential is more sensitive to the wave number than the screened one; this is unrelated to the orbital character. However, it is not a problem when we discuss qualitatively.
- [81] R. Cava, H. Takagi, B. Batlogg, H. Zandbergen, J. Krajewski, W. Peck, R. Vandover, R. Felder, T. Siegrist, K. Mizuhashi, J. Lee, H. Eisaki, S. Carter, and S. Uchida, *Nature (London)* **367**, 146 (1994).
- [82] W. H. Press, S. A. Teukolsky, W. T. Vetterling, and B. P. Flannery, *Numerical Recipes 3rd Edition: The Art of Scientific Computing*, 3rd ed. (Cambridge University Press, New York, NY, 2007).